Pt–Au Alloying at the Nanoscale

Valeri Petkov,*,[†] Bridgid N. Wanjala,[‡] Rameshwori Loukrakpam,[‡] Jin Luo,[‡] Lefu Yang,[‡] Chuan-Jian Zhong,[‡] and Sarvjit Shastri[§]

[†]Department of Physics, Central Michigan University, Mt. Pleasant, Michigan 48859, United States

[‡]Department of Chemistry, State University of New York at Binghamton, Binghamton, New York 13902, United States

[§]Advanced Photon Source, Argonne National Laboratory, Argonne, Illinois 60439, United States

S *Supporting Information*

ABSTRACT: The formation of nanosized alloys between a pair of elements, which are largely immiscible in bulk, is examined in the archetypical case of Pt and Au. Element specific resonant high-energy X-ray diffraction experiments coupled to atomic pair distribution functions analysis and computer simulations prove the formation of Pt–Au alloys in particles less than 10 nm in size. In the alloys, Au–Au and Pt–Pt bond lengths differing in 0.1 Å are present leading to extra structural distortions as compared to pure Pt and Au particles. The alloys are found to be stable over a wide range of Pt–Au compositions and temperatures contrary to what current theory predicts. The alloy-type structure of Pt–Au nano-particles comes along with a high catalytic activity for electrooxidation of methanol making an excellent example of the synergistic effect of alloying at the nanoscale on functional properties.

KEYWORDS: *High-energy resonant XRD, atomic pair distribution functions, reverse Monte Carlo modeling, structure of metallic nanoparticles, catalysis*
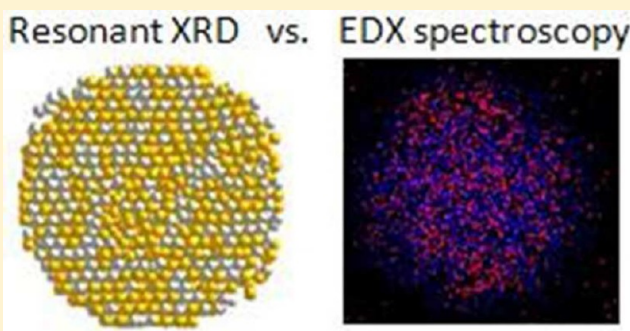
Bulk gold (Au) and platinum (Pt) are known as noble metals because they are very inert chemically with respect to gases and liquids. This special property of bulk Au and Pt has been employed in several applications in traditional medicine and electronics. With current technology moving rapidly toward smaller scales, Au and Pt have been increasingly produced in nanosized dimensions and explored for bio-medical,[1,2] optical,[3] magnetic,[2,4] and catalytic[5−8] applications. These recent studies have revealed that 1−10 nm particles of pure Pt, pure Au, Pt−Au mixtures, and Pt/Au mixtures with other mostly transition metals develop new properties that are quite different from those of the respective bulk metals and alloys. While good progress has been made in producing nanosized Au- and Pt-based materials and devices the understanding of why Pt and Au behave so differently when reduced to nanoscale dimensions is far less advanced. Questions about the nanosized Au and Pt atomic-scale structure ground state, and the possible formation of alloys between Au and Pt that are largely immiscible in bulk are still unsettled. In particular the picture of 1−10 nm sized Pt/Au particles has been evolving from featuring them as uniform pieces of face-centered cubic (fcc) lattices terminated with regular facets[9] to inhomogeneously strained and locally disordered yet fcc-like atomic arrangements[10,11] that some studies imply may[12,13] and others may not[14−17] form stable Pt−Au alloys. Progress in understanding these fundamental questions has been hindered by the lack of advanced analytical techniques that can deliver structure knowledge about 1−10 nm Pt−Au particles with both good atomic position accuracy and chemical specificity.

Here Au, Pt, and $Pt_xAu_{1−x}$ (x = 0.77, 0.51, 0.4, 0.2) particles are studied by resonant high-energy X-ray diffraction (XRD) coupled to atomic pair distribution functions (PDFs) analysis and computer simulations. This nontraditional experimental approach allows one to obtain a very clear picture of the nanoparticles (NPs) atomic-scale structure. In particular, we find that Pt and Au keep their bond distances almost unchanged from the bulk values resulting in extra structural distortions in the binary $Pt_xAu_{1−x}$ particles. In all particles, the structural distortions increase from the core toward the surface. Yet, similarly to the bulk, Pt and Au atoms arrange in an fcc-like pattern in both pure Pt and Au as well as in the binary $Pt_xAu_{1−x}$ particles. However, contrary to the bulk case[18] and to what current theory predicts,[14−16] we find that $Pt_xAu_{1−x}$ NPs exhibit a random alloy-type structure and do not segregate into a core−shell morphology even when annealed to temperature as high as 800 °C. This result is independently confirmed by energy dispersive X-ray spectroscopy (EDX) experiments. The random alloy-type structure of $Pt_xAu_{1−x}$ NPs endows them with high catalytic activity for electrooxidation of methanol

providing an excellent example of the synergistic effect of metal alloying at the nanoscale on functional properties.

Gold, platinum, and Pt–Au particles were synthesized by a modified two-phase method using aqueous solutions of $HAuCl_4$ and H_2PtCl_6. While in solution the particles were mixed with fine carbon powder. The carbon-supported Pt–Au particles were dried out and subjected to removal of the capping organic molecules in a tube furnace at 300 °C in 20% O_2/N_2 atmosphere for 1 h. Two batches of particles were prepared by further annealing at 400 and 800 °C, respectively, under 15% H_2/N_2 atmosphere for extra 2 h. The exact chemical composition of the particles was determined by direct current plasma-atomic emission spectroscopy and found to be Pt, $Pt_{0.77}Au_{0.23}$, $Pt_{0.51}Au_{0.49}$, $Pt_{0.40}Au_{0.60}$, $Pt_{0.20}Au_{0.80}$, and Au. More details of the preparation procedure are given in the Experimental and Modeling Methods. Transmission electron microscopy (TEM) studies (for details see the Experimental and Modeling Methods and Supporting Information Figure S1) showed that the particles are spherical in shape and with a narrow size distribution. The average size of the particles annealed at 400 °C was found to be 5.1(5) nm while that of the particles treated at 800 °C was 8.0(1.0) nm. The carbon-supported NPs were loaded into thin-walled glass capillaries with a diameter of 1.5 mm and subjected to synchrotron XRD measurements details of which are given in the Experimental and Modeling Methods. Typical for materials of nanosized dimensions the particles show rather diffuse XRD patterns with broad peaks (see Supporting Information Figure S2) rendering traditional, sharp Bragg peaks based atomic-scale structure analysis hardy applicable. As we[19−21] and others[22−24] have shown the task is greatly simplified if not the diffuse XRD patterns but their Fourier transform, the so-called atomic PDFs, are considered instead. Experimental atomic PDFs for the 5.1 nm particles studied here are shown in Figure 1a. Note that the atomic PDFs thus derived are usually called total in a sense that they show all distinct types of interatomic correlations in the respective materials. For the pure Au and Pt NPs, the total PDFs thus reflect the correlations between the only one chemical species present: Au–Au and Pt–Pt correlations, respectively. For the binary Pt_xAu_{1-x} NPs the total PDFs in Figure 1a reflect the correlations between the two chemical species present, that is, Au–Au, Au–Pt, and Pt–Pt correlations. Details of the total PDFs derivation are given in the Experimental and Modeling Methods.

As can be seen in Figure 1a, the total PDFs show a series of sharp peaks reflecting the presence of well-defined atomic coordination spheres in all NPs. For 5.1(5) nm particles the respective total PDFs should show physical oscillations up to distances of 5.1 nm. The experimental PDFs, however, decay to zero at distances of about 3.5 nm that indicates the presence of local structural disorder diminishing the NP's structural coherence length to distances shorter than their size. Both metallic[10,11] and nonmetallic[25,26] NPs are often found to show such disorder mostly due to surface relaxation effects. The PDFs for pure Pt and Au NPs have their first peaks positioned at distances of 2.76(1) and 2.86(1) Å, which are very close to the Pt–Pt and Au–Au bond lengths in bulk Pt and Au, respectively.[27] The position of the first peak in the total PDF for Pt_xAu_{1-x} NPs smoothly varies with x (see Figure 1b) from 2.78(1) for $x = 0.77$ to 2.84(1) Å for $x = 0.2$. The eventual presence of fine structure in that peak, that is, the eventual presence of distinct Pt–Pt and Au–Au bond lengths in Pt_xAu_{1-x} NPs is unclear since the XRD data (see the
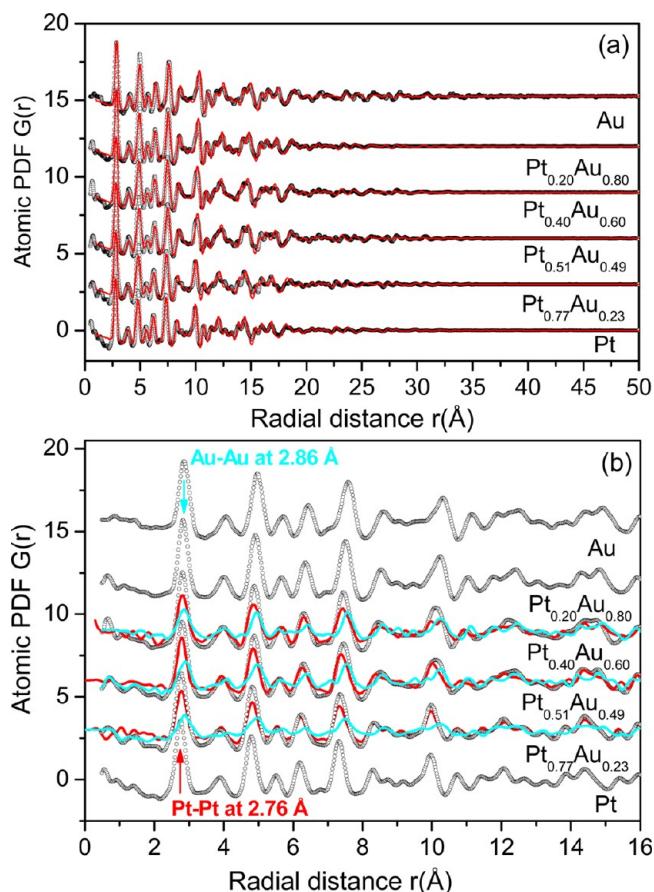

Figure 1. (a) Experimental (symbols) and model (line in red) atomic PDFs for 5.1(5) nm Au–Pt particles. The model PDFs are based on a fcc-type lattice as explained in the text. The respective goodness-of-fit factors (see eq 10 in the Experimental and Modeling Methods) are in the range of 18–20%. (b) Low r part of the experimental atomic PDFs for 5.1 nm Au–Pt particles (symbols). Experimental Pt differential PDFs (line in red) and Au–Au partial PDFs (line in cyan) are also shown. Arrows mark the positions of the Pt–Pt and Au–Au bond distances. The data sets are shifted by a constant factor for clarity.

Experimental and Modeling Methods and Supporting Information Figure S3) has been recorded to wave vectors of q_{max} = 24 Å^{-1} limiting the real space ($\Delta r = 2\pi/q_{max}$) resolution of the total PDF data to approximately 0.25 Å.

The experimental PDFs were first approached with a model based on the fcc-type lattice occurring in both bulk Pt and Au.[27] In this type of traditional crystallography constrained modeling,[28] a PDF for an infinite fcc lattice is first computed. Then each of the coordination spheres of the perfect lattice is broadened by a convolution with a Gaussian function to take into account the presence of thermal (Debye–Waller type) and static local atomic displacements in NPs. At the same time, the computed PDF is multiplied by a particle shape (spherical in our case) dependent function that is zero for distances longer than the size of the NPs being modeled. It is a simplistic approximation to the structure of real NPs but is useful since it allows one (i) to verify the type of their atomic ordering and (ii) to obtain a set of structural parameters (e.g., lattice constants and atomic displacement amplitudes) that may be compared directly with those for the corresponding bulk materials. Details of the computations are given in the Experimental and Modeling Methods. As can be seen in Figure 1a the experimental PDFs can be approximated reasonably well

Table 1. Lattice Parameter, *a*, and Mean-Square Atomic Displacements, *U*, As Resulted from Fitting the Total Atomic PDFs for 5.1 nm Pt−Au Particles with a Model Based on a fcc-Type Lattice[a]

	Pure Pt	$Pt_{0.77}Au_{0.23}$	$Pt_{0.51}Au_{0.49}$	$Pt_{0.4}Au_{0.6}$	$Pt_{0.2}Au_{0.8}$	pure Au
a (Å)	3.918(2)	3.941(2)	3.995(2)	4.005(2)	4.023(2)	4.077(2)
U (Å²)	0.016	0.021	0.025	0.022	0.018	0.016

[a]For reference, the lattice parameter of bulk fcc Pt is 3.924 Å and that for bulk fcc Au is 4.080 Å. No lattice parameter for crystalline Pt−Au alloys is known since Pt and Au are largely immiscible in bulk.

(goodness-of-fit factors of the order of 18−20%) with models based on an fcc-type lattice indicating that the NPs studied here exhibit the structure type of their bulk counterparts. The refined NP's "fcc lattice parameters" and atomic mean square displacements are summarized in Table 1. The lattice parameters of $Pt_xAu_{1−x}$ NPs evolve smoothly with the relative Pt content, *x*, between the values for pure Pt and Au NPs which, in turn, are pretty close to those found in bulk Pt and Au.[27] The atomic displacement amplitudes, however, do not evolve smoothly with the relative Pt/Au content. They are much larger in the $Pt_xAu_{1−x}$ NPs than in the pure Pt and Au NPs indicating that the binary NPs suffer extra structural disorder, and disorder is known to affect the properties of NPs very substantially.[29] To reveal the origin of this extra disorder and how exactly Pt and Au atoms are arranged with respect to each other across the NPs, structure data sensitive to the Au and Pt species are needed. Sensitivity to the chemical type of the atomic species may be added by employing spectroscopic techniques such as extended X-ray absorption fine structure spectroscopy (EXAFS) or imaging techniques such as high-angle-annular-dark field scanning transmission electron micros-copy (HAADF-STEM). The EXAFS technique is very useful but yields information on the atomic ordering extending out to 5−6 Å only. Thus, for example, an EXAFS experiment would hardly distinguish between a hexagonal and fcc-type atomic ordering in NPs since both show first and second coordination spheres of 12 and 6 atoms, respectively. Besides, EXAFS signals of species that, like Pt and Au, are neighbors in the Periodic Table overlap and are not trivial to disentangle.[30] Likewise, HAADF-STEM can reveal well compositional variations in NPs with atomic resolution when the chemical species probed are not very close to each other in atomic numbers.[31,32] However, like any other images HAADF-STEM images are just a projection down an axis and so not very sensitive to the atomic ordering inside nanoparticles. We overcame the difficulty by employing the so-called resonant XRD, which involves measuring two XRD data sets close to but below the absorption edge of an atomic species, taking the difference between these two data sets, and Fourier transforming it into a quantity called a differential atomic PDF.[33] Similarly to EXAFS results, the differential PDF reflects only correlations relative to the element whose absorption edge is probed. However, unlike EXAFS, it shows these correlations up to the longest interatomic distances to which they extend. In the past resonant XRD experiments have been conducted on relatively low-energy (20 to 30 keV) K edges of transition metals in bulk amorphous alloys.[34−36] The feasibility of resonant XRD on high-energy (70 to 80 keV) K edges of noble metals in less than 10 nm in size particles diluted in solution has been documented by us very recently.[37] Here we extend these studies to NPs supported on very fine carbon powders (see the Experimental and Modeling Methods), where the NPs mass loading was kept as low 10% (i.e., approximately $5 \times 10^{−5}$ mg/cm²) meeting the requirements of real life applications. In particular, carbon-

supported binary NPs treated at 400 °C with a composition of $Pt_{0.77}Au_{0.33}$, $Pt_{0.51}Au_{0.41}$, and $Pt_{0.40}Au_{0.60}$ were subjected to resonant XRD experiments conducted at the Pt Kα edge. The choice of Pt Kα versus Au Kα edge does not give any particular advantages or disadvantages. We could have conducted resonant XRD on both edges but resorted to only one due to experimental time limitations. From XRD patterns collected at two energies below the Pt Kα edge, Pt differential structure factors were obtained (e.g., see Supporting Information Figure S3a). Those were Fourier transformed into Pt differential PDFs shown in Figure 1b. Since the Kα edge of Pt species was probed these differential atomic PDFs contain contributions from atomic pairs involving Pt−Pt and Pt−Au atomic pairs only. Furthermore, by using the recently introduced MIXSCAT approach[38] the Au−Au correlations in the $Pt_{0.77}Au_{0.23}$, $Pt_{0.51}Au_{0.49}$, and $Pt_{0.40}Au_{0.60}$ NPs were also obtained from the respective experimental total PDFs and Pt differential PDFs data. Basically the MIXSCAT approach involves appropriately weighing two experimental atomic PDFs and taking a difference between them to eliminate particular atomic pair correlations that appear in the two PDFs but with different weight contributions. Partial Au−Au PDFs obtained in this way are also shown in Figure 1b. Details of the resonant high-energy XRD experiments, Pt differential, and Au−Au partial PDFs derivations are given in the Experimental and Modeling Methods.

As can be seen in Figure 1b, all three Pt differential PDFs have their first peak at a distance close to the position of the first peak in the PDF for pure Pt NPs. For example, the Pt differential for $Pt_{0.77}Au_{0.23}$ in which the contribution of Pt−Au pairs is relatively low has its first peak at 2.77 Å. The Pt differential for $Pt_{0.51}Au_{0.49}$ in which the contribution of Pt−Au pairs is much higher has its first peak at 2.79 Å. The Pt differential for $Pt_{0.40}Au_{0.60}$ in which the contribution of Pt−Au pairs is even higher has its first peak at 2.80 Å. The slight shift from 2.77 to 2.79 and then to 2.80 Å can be explained with the increasing contribution of Pt−Au pairs to the respective differential PDFs. As explained below, that contribution comes about at distances longer than 2.76 Å. Furthermore, all three Au−Au partial PDFs have their first peak at exactly the same distance of 2.86 Å that is very close to the position of the first peak in the PDF for pure Au NPs. The result indicates that Au−Au and Pt−Pt bond lengths in 5.1(5) nm carbon supported Pt−Au NPs do not take some average values that scale with the Pt/Au relative content. Rather they remain very close to the respective bond lengths of 2.76(1) and 2.86(1) Å in pure Pt and Au, respectively. Understandably, the Pt−Au bond lengths are in between these two values, that is, close to 2.81 Å. Thus when two metal atoms of different dimensions are mixed together in an fcc-type structure the latter inevitably will have to distort locally to accommodate them. This may well explain why the atomic displacement amplitudes in $Pt_xAu_{1−x}$ NPs (see Table 1) are substantially larger than those in pure Pt and Au NPs. A similar effect has been observed in

semiconductor alloys.[39] A question then arises. How do the size-different Pt ($Pt_{diamater}$ = 2.76 Å) and Au ($Au_{diameter}$ = 2.86 Å) atomic species arrange themselves across the 5.1(3) nm NPs? Is it by (i) forming an fcc-type alloy or (ii) phase segregating in a core−shell type morphology as current theory[14−16] predicts? To answer it, we built structure models featuring NPs of real size (5.1 nm) and shape (spherical; see Supporting Information Figure S1) that are able to incorporate chemical order−disorder effects extending beyond a single unit cell of an fcc lattice. The models were built by reverse Monte Carlo simulations (for details see the Experimental and Modeling Methods) and tested against the experimental total and Au−Au partial PDFs data that are very sensitive to the spatial arrangement of the atomic species in $Pt_xAu_{1−x}$ NPs. Moreover, Au−Au partial PDFs are able to pinpoint the spatial arrangement of only Au chemical species across the NPs adding very much needed chemical specificity.

Figure 2 exemplifies the differences between the outcomes of infinite lattices-constrained and finite size, real shape NP's
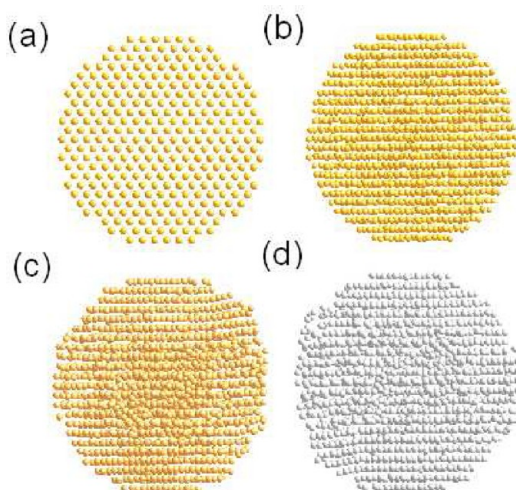

Figure 2. Cross sections of monometallic 5.1 nm particles of approximately 5000 atoms (a) as cut out from a perfect fcc lattice; (b) same as (a) but with all atoms exhibiting mean-square displacements of 0.025 Å^2; (c) model for Au particles as refined against the respective experimental PDF data by reverse Monte Carlo simulations; (d) model for Pt particles as refined against the respective experimental PDF data via reverse Monte Carlo simulations. The RMC derived models reveal an fcc-type ordering that is nonuniform in a sense that is more disordered close to the NP's surface.

structure modeling. In Figure 2a, a 5.1 nm in diameter, 5000 atom fragment of a perfect fcc lattice of pure Au is shown. Next to it (see Figure 2b) is the same fragment where all atoms have been displaced about their positions with an average square amplitude of 0.025 Å^2 suggested by the infinite lattice-constrained structure modeling (see Table 1). A model PDF computed from that configuration (see Supporting Information Figure S4) decays to zero exactly at distances of about 5.1 nm but shows peaks that are way too sharp when compared to the peaks in the respective experimental PDF data. In other words, a model where the atoms are constrained by translation vectors of a periodic lattice and so have the same displacement amplitudes is not a very realistic representation of the atomic ordering in real NPs. When the atomic positions are refined individually against the experimental PDF data by reverse Monte Carlo (RMC) simulations and at the same time the

energy of the model is optimized by minimizing pairwise (Lenard-Jones type) atomic interactions the configurations shown in Figure 2c,d result. Not surprisingly model PDFs computed from the RMC refined models fit the experimental PDFs much better that the model PDFs computed from the crystallography constrained models (see Supporting Information Figure S4). The models resulted from the reverse Monte Carlo simulations show that the fcc-type atomic ordering in 5.1 nm NPs (see Figure 2c for pure Au and Figure 2d for pure Pt NPs) is not uniform across their diameters. Atoms at the inner part of the NPs show less mean square displacements than atoms closer to the NP's surface. The latter may deviate from their average positions in a perfect fcc-lattice by as much as 0.06 Å^2, mostly in a direction perpendicular to the NP's surface. This finding is fully in line with the results of other independent studies on NPs.[11,25] The nonuniformity in the NP's atomic-scale structure may have important implications on their functional properties and in particular the catalytic ones. Because the NPs's surface is not terminated by families of flat atomic planes of a periodic fcc lattice but is uneven, the catalytic activity of NPs may be very different from that of the respective bulk solids.[40]

The RMC refined models for pure Au and Pt NPs were used to produce model configurations for $Pt_xAu_{1−x}$ NPs where Au and Pt atoms show various patterns of chemical order−disorder effects. Those models are shown in Figure 3 and used to compute the model Au−Au partial PDFs shown in Figure 4. The spatial arrangements of the Au atoms in the models shown in Figure 3 are very different and so are the respective Au−Au partial PDFs. In particular, if Au atoms were to segregate in the core of the NPs (see Figure 3, middle section) the correlations between those Au atoms would be just like in a fcc cluster with the size of the NP's core, that is, they would be very limited in their spatial extent (see Supporting Information Figure 5 for example). If Au atoms were to segregate at the surface of 5.1 nm NPs, they would form a few atomic layers thick shell. These Au atoms would then have quite a few first and second like (i.e., Au−Au) neighbors and very few more distant like neighbors. As a result the peaks in the respective Au−Au partial PDF would show a pronounced steplike drop in intensity beyond the second atomic neighbor distances (see Supporting Information Figure S5 for example). If Au atoms were well mixed with Pt atoms throughout the NPs (see Figure 3, right section) they would have much less like (i.e., Au−Au) neighbors in all coordination spheres, starting with the first, rendering all peaks in the respective Au−Au partial PDFs with a greatly but uniformly diminished intensity. As can be seen in Figure 4, only structure models where Au and Pt atoms are well mixed together throughout the NPs produce Au−Au partials PDFs that are consistent with the experimental data. The result shows that the $Pt_xAu_{1−x}$ NPs studied here do not phase segregate contrary to their bulk counterparts. A confirmation of our finding comes from independent HAADF-STEM and EDX spectroscopic results shown in Figure 5. As can be seen in the figure, the Au and Pt species are rather uniformly distributed across the spherical in shape nanoparticle clearly not forming a core−shell type pattern. Indeed the experimental EDX map of Pt and Au species distribution (see Figure 5, right) and the RMC constructed model for a random alloy $Pt_{0.51}Au_{0.49}$ particle (see Figure 3, middle of the right column) show a remarkable resemblance. The difference is that the EDX is just a map mostly sensitive to the NP's surface while the coordinates of all
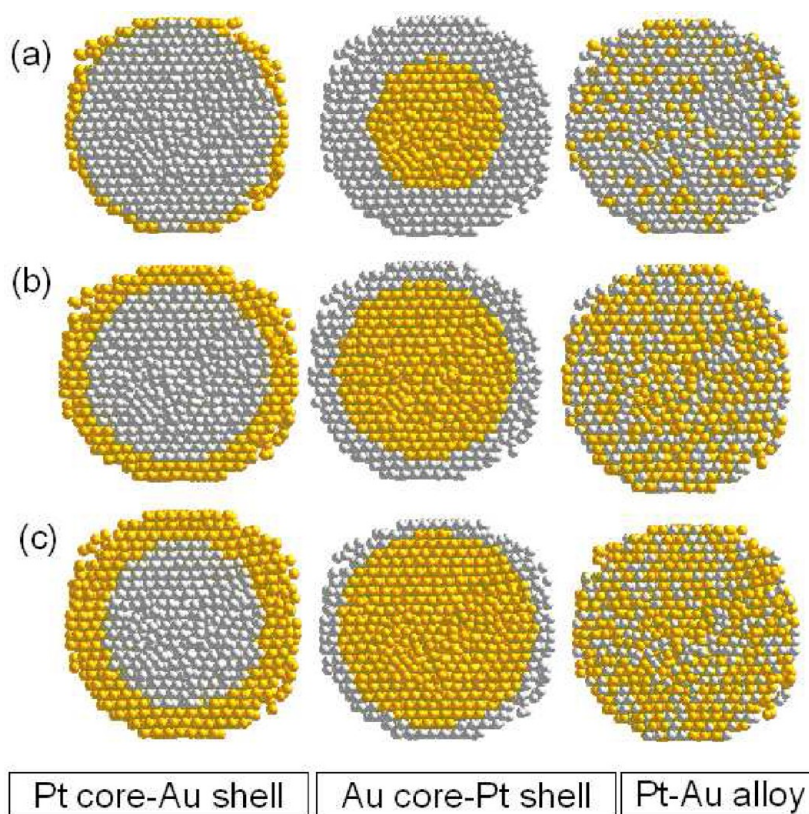
Figure 3. Cross sections of 5.1 nm Pt−Au particles (about 5000 atoms) with a core−shell and random alloy structure: (a) $Pt_{0.77}Au_{0.23}$; (b) $Pt_{0.51}Au_{0.49}$; and (c) $Pt_{0.40}Au_{0.60}$. Pt atoms are in gray, Au in yellow. The ratio of Pt/Au atoms in the models exactly reflects the respective NP's chemical composition. Note the model structures represent assembly averaged structural features of all particles sampled by the X-ray beam (1 mm by 1 mm in the present experiments) in a way the structure models generated by traditional powder XRD represent an assembly average of all polycrystallites sampled by the X-ray beam (again typically with a few mm^2 footprint) in those experiments. Comparing particle's assembly averaged structure models to particle's assembly averaged properties (e.g., catalytic) puts structure−property relationship exploration on the same footing.

5000 atoms from the RMC model are known and can be used for computing and predicting of NP's properties.

Experimental total and Au−Au partial PDFs were obtained for the 800 °C processed $Pt_xAu_{1−x}$ NPs as well. Those are shown in Supporting Information Figure S6. The PDFs for the 800 °C processed particles show physical oscillations to distances somewhat longer than those seen in the PDFs for the 400 °C processed samples. This reflects the fact that 800 °C processed particles have a somewhat larger size (8.0 nm) than the 400 °C processed particles (5.1 nm) Otherwise the PDFs for the 800 °C processed NPs are rather similar to those for the 400 °C processed NPs showing that the former, just like the latter, possess an fcc-type ordering. Furthermore, all peaks in the partial Au−Au PDFs for the 800 °C processed $Pt_xAu_{1−x}$ NPs are with greatly but uniformly diminished intensity which is characteristic of random type Pt−Au alloys. Obviously the alloying of Pt and Au occurs not only within a wide range of Pt−Au concentrations but is also stable in NPs of different sizes and over a broad temperature range. Common wisdom would suggest that Au and Pt atoms that have different sizes and surface energy would tend to segregate, especially at elevated temperatures, into a single Pt_core-single Au_shell morphology to relieve the atomic size mismatch strain energy and reduce the NP's overall surface tension. Indeed this is exactly what current theory predicts[14−16] for Pt−Au particles of sizes, compositions and a temperature range explored in the present study. Also, single core-single shell type morphology is what has been observed experimentally in less than 10 nm in size Pt-transition metal binary NPs.[41] However, as our results show nanosized random Pt−Au alloys are formed instead. Note that these alloys are not kinetically trapped but are thermodynamically quite stable since, as other studies have shown,[9,17] the mobility of Pt and Au atoms is quite high in the temperature range of 400−800 °C explored here. Also, our own studies on fresh and aged samples have found that the alloying characteristics of approximately 5 nm in size Au−Pt particles remain unchanged even after a shelving time of more than 5 years. Evidently, the alloy state of 5−8 nm Pt−Au NPs revealed by our resonant high-energy XRD studies and confirmed by EDX spectroscopy bears the characteristics common to stable ground-structure states. Usually such states come with a distinct set of physicochemical properties which is the case with the PtAu NPs as discussed below. This is a prime demonstration of "the plenty of room for generating new structures at the nanoscale" concept.[42] Our experimental finding of a complete suppression of the miscibility gap in the Pt−Au system confined to nanoscale (less than 10 nm) dimensions may only encourage theory to look beyond its current realms. Taking into account the largely neglected presence of nonuniform structural disorder (see Figure 2), excess strain,[11,25] and the stemming from them breaking[10,26] of the lattice periodicity in 1−10 nm NPs may be worthwhile pursuing as some studies suggest.[43−46]

The ability to produce structurally nonuniform but chemically uniform NPs of a wide range of $Pt_xAu_{1−x}$ compositions is quite valuable for catalysis applications. Among other metals Pt
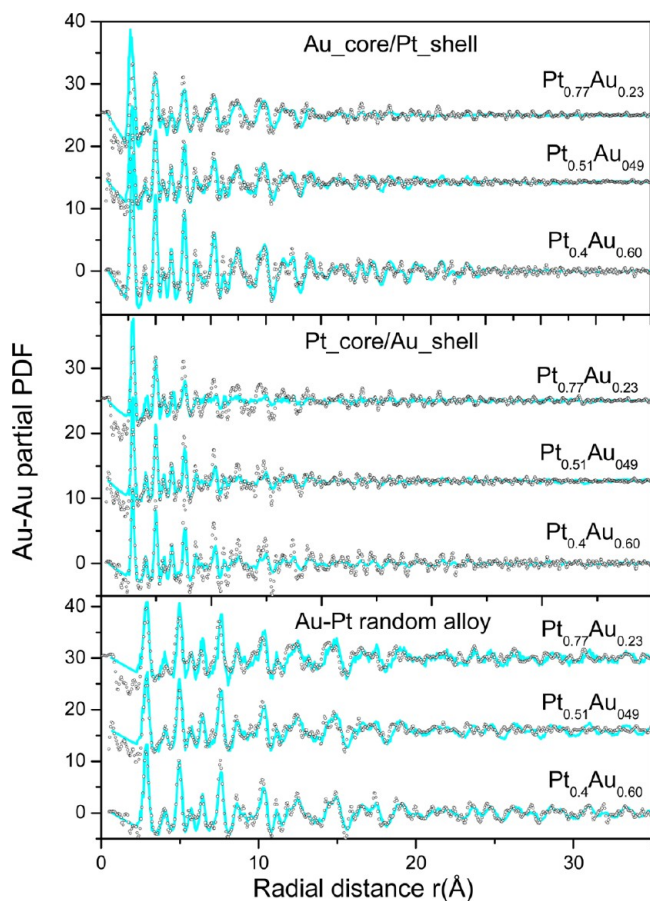
Figure 4. Experimental (symbols) and model (line in cyan) Au–Au partial PDFs for 5.1 nm Pt–Au particles. The model PDFs are computed from the atomic configurations in Figure 3. The data sets are shifted by a constant factor for clarity. Au_core/Pt_shell model Au–Au PDFs show first peaks that are too strong in intensity than the peaks in the respective experimental Au–Au PDFs, and also decay to zero much faster than the experimental data. Peaks in the Au–Au PDFs for Pt_core/Au_shell model show characteristic step-down loss in intensity at short interatomic distances that is inconsistent with the behavior of the experimental data. Au–Pt random alloy model Au–Au PDFs agree with the experimental data in good detail.
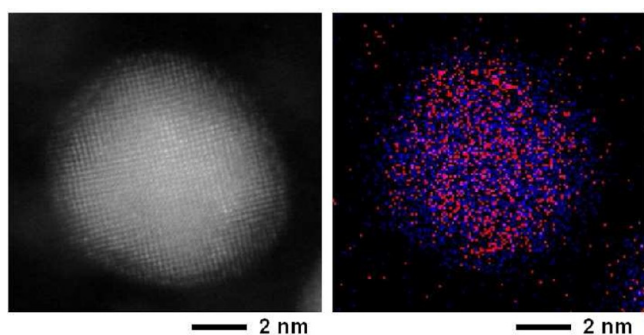

Figure 5. HAADF-STEM image of $Pt_{0.51}Au_{0.49}$ nanoparticle supported on carbon. The particle has a fairly spherical shape and relatively smooth surface (left); EDX spectroscopic composition map showing a uniform distribution of the two metals (red dots, Pt; blue dots, Au). The EDX map resembles very much the RMC constructed structure model for 5.1 nm particles shown in Figure 3 (right column, in the middle).

shows best catalytic properties for many industrially important reactions and devices such as fuel cells and sensors.[47−50] Unfortunately Pt is very rare in nature which precludes its large scale usage in catalysis applications. Very large effort is underway to find nanosized catalysts that are as much Pt free as possible yet show its superb properties. Mixing Pt with other, more abundant metals, such as Au, is one way to go. In Figure 6, data for the Pt mass normalized catalytic activity of carbon-
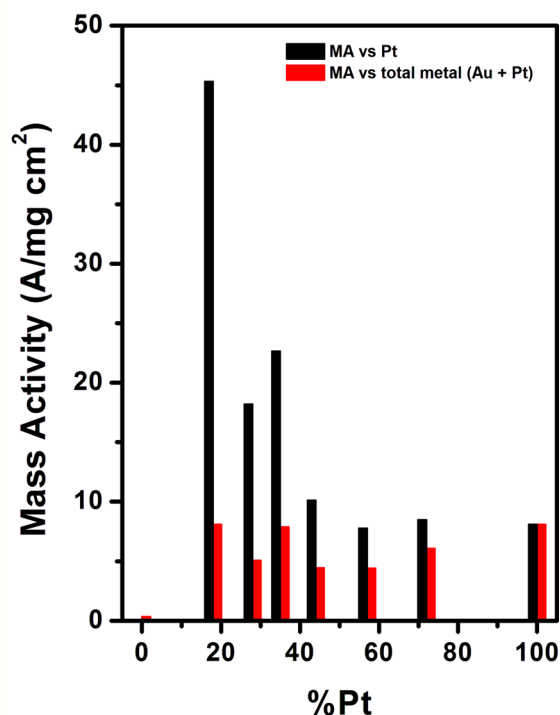

Figure 6. Electrocatalytic activities in terms of the total Pt metal mass (black bars) and the total Pt and Au metals mass (red bars) for methanol oxidation reaction in basic electrolyte (0.5 M KOH + 0.5 methanol) of carbon supported 5.1 nm Pt_xAu_{1-x} particles treated at 400 °C compared to those of pure Au and Pt particles. The error margin in the data is ($\pm$)0.5 A/mg cm^2.

supported Pt_xAu_{1-x} NPs treated at 400 °C for methanol oxidation reaction in a basic electrolyte are shown. Details of the catalytic measurements are given in the Experimental and Modeling Methods. As can be seen in the figure, alloying Pt with Au up to approximately $Pt_{0.20}Au_{0.80}$ keeps the total mass catalytic activity of the NPs very high. In terms of a relative Pt-specific mass activity it is even maximized at Au concentration of 60−80%. Note that (i) pure Au NPs are not active for this reaction so that the high catalytic activity of Pt_xAu_{1-x} NPs may not be explained as a simple linear combination of the properties of Au and Pt metals, (ii) the size and shape (e.g., compare Figure 5a with Supporting Information Figure S1c) of all NPs across the 400 °C Pt_xAu_{1-x} series are very much the same precluding NP's size and shape changing effects[51] as an explanation, and (iii) the Au–Au and Pt–Pt bond lengths do not change much so an explanation of the high catalytic activity in terms of bond lengths contraction[52−55] is not relevant here either. Other factors to consider are the effect of fine geometric features on the NPs surface and of charge redistribution coming from the chemical alloying. High-resolution images (see Figure 5a and Supporting Information Figure S1c) give little evidence

for large-scale geometric features (e.g., voids etc) at the Au–Pt NPs surface. The particles are with relatively smooth but, as out RMC modeling shows, uneven surfaces that likely have small steps (at least of the order of 0.3 Å) and kinks that may be catalytically very active sites. The charge transfer may come from the difference in the electronegativity of Pt and Au. Mixing of Pt and Au atoms results in subtle Pt-to-Au net charge transfer as found in other studies.[55,56] Such charge transfer may be expected to occur throughout the alloy $Pt_xAu_{1−x}$ NPs modifying the electron density distribution of all atoms and so affecting[57−65] their catalytic activity. In particular, the increase in the d-band vacancy at the Pt sites may facilitate the transfer of intermediate CO-like species toward the neighboring Au sites and, hence, facilitate the formation of the carbonate $(CO_3^{2−})$ product in the oxidative reaction of methanol. To check for possible charge transfer between Pt and Au atomic species we conducted X-ray photo absorption spectroscopy experiments (XPS). Results are summarized in Table 2. Overall,

Table 2. Comparison of the XPS Experiments Determined Binding Energy (BE) Values (in eV) for $Pt_{0.77}Au_{0.23}$/C and $Pt_{0.51}Au_{0.49}$/C Processed at 400 and 800 °C

XPS bands	$Pt_{0.77}Au_{0.23}$/C		$Pt_{0.51}Au_{0.49}$/C	
	400 °C (BE)	800 °C (BE)	400 °C (BE)	800 °C (BE)
Au $4f_{5/2}$	88.08	88.08	87.68	87.72
Au $4f_{7/2}$	84.40	84.40	84.00	83.97
Pt $4f_{5/2}$	75.05	74.90	74.59	74.62
Pt $4f_{7/2}$	71.75	71.65	71.32	71.52

the binding energy (BE) values for Au 4f peaks are very close to the values known for bulk Au (for $Pt_{0.51}Au_{0.49}$/C) or slightly higher than bulk Au (for $Pt_{0.77}Au_{0.23}$/C). There is also little change in the binding energy with the change of NPs treatment temperature. This particular XPS experiment did not show an observable shift of the binding energy for Au 4f toward lower values. The reason could be that these subtle changes are buried in the broad XPS peak envelopes, necessitating a further, more detailed spectral analysis to reveal the expected subtle shift in the binding energies of Pt and Au. Note broadened XPS peaks are to be expected for NPs that, like ours, exhibit a great deal of structural disorder, in particular close to their surface.

In any case, the mixing of Pt and Au in random-type alloys comes along with excellent catalytic properties of $Pt_xAu_{1−x}$ NPs over a broad range of x values. Those properties are largely impossible to comprehend in terms of the single Pt_core-single Au_shell structure model suggested by theory.

Indeed tuning the degree of chemical ordering-disordering in 1−10 nm metal NPs emerges as a very efficient way to improve their catalytic activity.[50,66−74] Resonant high-energy XRD and differential atomic PDFs analysis can be invaluable in this effort by providing much needed structural information with both high spatial resolution and chemical specificity. In particular, as the present studies show bond lengths mismatch as little as 0.1 Å can be clearly resolved by conducting resonant XRD on high-energy K edges of metal species. Such a very high resolution can greatly facilitate revealing the exact origin of excess strain and disorder in metallic NPs. Note this is virtually impossible to be achieved by traditional high energy X-ray or neutron diffraction since it would require collecting data to wave vectors as high as 60−70 Å$^{−1}$. Furthermore, resonant high-energy XRD and differential PDFs analysis can help greatly in revealing the true nature of chemical ordering even when the chemical

species in NPs are very close in atomic numbers which renders other traditional characterization techniques inapplicable. An added value is the fact that resonant high-energy XRD can be done on small amounts (e.g., down to fractions of mg) of NPs as loaded on supports or in solutions facilitating in situ studies when necessary. As such the technique is a valuable complement to TEM, HAADF-STEM, XPS and several other experimental techniques that are already well established in the field of catalysis.

On a more general note, advancing science and technology will keep generating nanosized materials with increasingly complex structure and chemistry. The 1−10 nm range of sizes appears of a particular interest to biomedical, catalytic, magnetic, and optical applications.[1−8] Materials confined to such small sizes may not necessarily have bulk analogues nor be quite expected to exist from first principles. This research effort may only benefit from advanced analytical tools such as resonant high-energy XRD coupled to differential PDFs analysis that can deliver precise knowledge about the atomic and chemical ordering (e.g., see Figure 3, right) across the NPs allowing properties targeted for improvement to be considered in terms of a proper atomic-scale structure basis and so better utilized. Also, structure models resulting from such experimental studies may serve as a basis for testing and improvement of the predictive power of theory and so help turn the still largely trial-and-error approach to developing 1−10 nm sized materials into a smart engineering endeavor.

Experimental and Modeling Methods. *Nanoparticle Samples Preparation.* Au, Pt, and Au–Pt NPs were synthesized by a modified two-phase method. It involved transferring of $AuCl_4^−$ and $PtCl_6^{2−}$ from aqueous solution of $HAuCl_4$ and H_2PtCl_6 into toluene using tetraoctylammonium bromide as a phase-transfer reagent. Thiols (e.g., decanethiol) or amine (e.g., oleylamine) compounds were added to the organic solution as NPs capping agents. An excess of aqueous $NaBH_4$ was slowly added for the reduction reaction. The resulting NPs were collected by removing the toluene solvent, washed in ethanol, and redispersed in hexane. Carbon black obtained from Cabot was used as NP's support. The carbon black was first pretreated by suspending in hexane and sonicated for 6 h at room temperature. A controlled amount of Au, Pt, or Au–Pt alloy nanoparticles was added into the suspension. The suspension was sonicated for another 30 min, followed by stirring overnight. Thus prepared carbon-supported Au, Pt, and AuPt particles were collected and dried under N_2. Typical NPs mass loading on the carbon support was about 10% (i.e., approximately $5 \times 10^{−5}$ mg/cm^2). The carbon-supported PtAu NPs were first annealed in a tube furnace at 300 °C under 20% O_2/N_2 for 1 h during which the capping molecules were completely removed as evidenced by complementary FTIR and XPS analyses. Then two batches of NPs were prepared by further annealing at 400 and 800 °C under 15% H_2/N_2 atmosphere for another 2 h each. The exact Au, Pt and AuPt NP's compositions were determined by direct current plasma-atomic emission spectroscopy and found to be Pt, $Pt_{0.77}Au_{0.23}$, $Pt_{0.51}Au_{0.49}$, $Pt_{0.40}Au_{0.60}$, $Pt_{0.20}Au_{0.80}$, and Au .

Nanoparticles' Size and Shape Characterization. The size and shape of nanoparticles were estimated using a 100 keV Hitachi H-7000 transition electron microscope. For the TEM measurements, the NPs were dispersed in hexane and then drop cast onto a carbon-coated copper grid followed by hexane/solvent evaporation in air at room temperature. TEM studies (see Supporting Information Figure 1) showed that the

NPs are spherical in shape and with a narrow size distribution. The average size of the NPs annealed at 400 °C was found to be 5.1(5) nm while that of the NPs treated at 800 °C was 8.0(1.0) nm.

Nanoparticles' Catalytic Properties Measurements. Glassy carbon (GC) disk (geometric area, 0.07 cm^2) was used as electrode for loading the catalyst on the surface. The catalyst ink was prepared by suspending 1.0 mg of particles in 1 mL of 0.25% Nafion solution and sonicating for 15 min. The suspension was then quantitatively transferred to the surface of the polished GC disk. The electrodes were dried overnight at room temperature. The measurement of the electrocatalytic activity employed the cyclic voltammetric (CV) method and was performed using a microcomputer-controlled electro-chemical analyzer (CHI600a, CH Instruments). The experiments were carried out in a three-electrode electrochemical cell at room temperature. A representative CV curve showing the electrocatalytic oxidation of methanol on a AuPt catalyst is shown in Supporting Information Figure S7. All electrolytic solutions were deaerated with high-purity argon or nitrogen before the measurement. The CV potentials are given with respect to the reference electrode of Ag/AgCl saturated with KCl. The active area of the catalysts in terms of the exposed Pt sites was determined by CV measurements in the hydrogen adsorption/desorption potential region in an acidic electrode. More details are given in ref 73.

Synchrotron X-ray Diffraction Experiments and Atomic PDFs Derivation. The experiments were carried out at the 1-ID beamline of the Advanced Photon Source at the Argonne National Laboratory. All samples were measured with X-rays of energy 78.070 keV which is 325 eV below the K absorption edge of Pt. The respective XRD patterns are given in Supporting Information Figure S2. A pure carbon sample not loaded with NPs was also measured and used as a reference "background" sample. In addition, the $Pt_{0.77}Au_{0.23}$, $Pt_{0.51}Au_{0.49}$, and $Pt_{0.40}Au_{0.60}$ samples annealed at 400 and 800 °C were measured with X-rays of energy 78.370 keV that is 25 eV below the K adsorption edge of Pt (see Supporting Information Figure S3a). The beam was delivered by a combination of a bent double-Laue premonochromator, collimating refracting lenses and a four crystal high-energy resolution (ΔE = 8 eV) monochromator.[75] The monochromator setup was calibrated and occasionally checked during data collection for stability against sub-eV energy drifts using the K absorption edge of a pure Pt foil in transmission. Scattered X-rays were collected by a single, intrinsic Ge detector coupled to a multichannel analyzer. Few energy windows, covering several neighboring channels, were set up to obtain counts integrated over specific X-ray energy ranges during the data collection. These energy windows covered: the elastic/coherent intensity only; the elastic, inelastic/incoherent (Compton), and Pt K_β fluorescence intensities all together; the Pt $K_{\alpha1}$ and $K_{\alpha2}$ fluorescence; and the total intensity scattered into the Ge detector. Integrated counts within these ranges were collected several times scanning up to wave vectors of 24 Å^{-1} and then averaged to improve the statistical accuracy. The integrated range of only elastically scattered X-ray photons with energy of 78.070 keV was further corrected for detector dead time, sample absorption and background/pure carbon scattering. The so corrected XRD data was reduced to structure factors defined as

$$S(q) = 1 + \frac{[I^{coh}(q) - \sum c_i |f_i(q)|^2]}{|\sum c_i f_i(q)|^2} \quad (1)$$

where c_i and $f_i(q)$ are the atomic concentration and X-ray scattering factor respectively for the atomic species of type i. The structure factors were Fourier transformed into atomic PDFs as follows

$$G(r) = \frac{2}{\pi} \int_{q=0}^{q_{max}} q[S(q) - 1]\sin(qr)dq \quad (2)$$

where q is the magnitude of the wave vector ($q = 4\pi \sin \theta/\lambda$), 2θ is the angle between the incoming and outgoing X-rays, and λ is the wavelength of the X-rays used.[19−23] The so-derived atomic PDFs are shown in Figure 1a. Usually they are called "total" PDFs in a sense that they reflect all distinct types of interatomic correlations in the material studied. In particular, for a material comprising n atomic species the total atomic PDF is a weighted sum of $n(n + 1)/2$ partial PDFs, $G(r_{ij})$, that is

$$G(r) = \sum_{i,j} w_{ij} G_{ij}(r) \quad (3)$$

where w_{ij} are weighting factors depending on the concentration and scattering power of the particular atomic species as follows

$$w_{ij} = \frac{c_i c_j f_i(Q) f_j(Q)}{[\sum c_i f_i(Q)]^2} \quad (4)$$

Therefore, for the pure Au and Pt NPs studied here the experimental total PDFs reflect the correlations between the only one chemical species present: Au−Au and Pt−Pt correlations, respectively. For the Pt−Au alloy, NPs in the experimental total PDFs in Figure 1a reflect the correlations between the two chemical species present, that is, Au−Au, Au−Pt, and Pt−Pt correlations.

Next, only the elastically scattered from the $Pt_{0.77}Au_{0.23}$, $Pt_{0.51}Au_{0.49}$, and $Pt_{0.40}Au_{0.60}$ NPs intensities collected with 78.370 keV X-rays were subtracted out from the elastically scattered intensities collected with 78.070 keV X-rays. The difference intensity is quite substantial as exemplified in Supporting Information Figure S3b and is entirely due to the substantial change in the dispersion corrections (see Supporting Information Figure S3a) to the atomic scattering factors of the Pt species only. The difference intensities were used to derive the so-called Pt differential structure factors[33,37]

$$DS(q)_{Pt} =$$
$$\frac{I^{coh}(q, E_1) - I^{coh}(q, E_2) - [\langle f^2(E_1)\rangle - \langle f^2(E_2)\rangle]}{\langle f(E_1)\rangle^2 - \langle f(E_2)\rangle^2} + 1 \quad (5)$$

where E_1 and E_2 denote the data sets collected with X-rays of 78.070 and 78.370 keV energy, respectively, and the atomic scattering factors $f(E) = f_o(q) + f'(q, E) + if''(q, E)$ are evaluated with the respective for the two energies dispersion corrections f' and f''.[37] The obtained Pt differential structure factor for $Pt_{0.51}Au_{0.49}$ NPs is shown in Supporting Information Figure S3c as an example. The corresponding Pt differential atomic PDF, $DG(r)_A$, was obtained via a Fourier transformation as follows:

$$DG(r)_{Pt} = \frac{2}{\pi} \int_{q=0}^{q_{max}} q[DS(q)_{Pt} - 1]\sin(qr)dq \quad (6)$$

where q_{max} extends to 24 Å^{-1}. Note, since only the scattering form factor of Pt atoms changed significantly, this differential atomic PDF contains contributions from atomic pairs involving Pt-i type atoms only, that is

$$DG(r)_{Pt} = \sum_i \Delta w_{Pt-i} G_{Pt-i}(r) \tag{7}$$

where

$$\Delta w_{Pt-i} = \frac{c_{Pt} c_i \ Re[f_i(f^*_{Pt}(E_1) - f^*_{Pt}(E_2)]}{\langle f(E_1) \rangle^2 - \langle f(E_2) \rangle^2} \tag{8}$$

and $f^*(E)$ is the complex conjugate of $f(q)$ and i = Pt, Au. The Pt differential atomic PDF for Pt$_{0.51}$Au$_{0.49}$ NPs is shown in Figure 1b together with the Pt differential PDFs for Pt$_{0.77}$Au$_{0.23}$, and Pt$_{0.40}$Au$_{0.60}$ NPs that were obtained in a similar manner.

Furthermore, by using the recently introduced MIXSCAT approach[38] the Au−Au correlations in the Pt$_{0.77}$Au$_{0.23}$, Pt$_{0.51}$Au$_{0.49}$ and Pt$_{0.40}$Au$_{0.60}$ NPs were also obtained from the experimental total PDF and Pt differential PDF data. Basically the MIXSCAT approach involves appropriately weighing two experimental atomic PDFs and taking a difference between them to eliminate particular atomic pair correlations that appear in the two PDFs but with different weight contributions.[38] Following the MIXSCAT approach the Pt−Pt and Pt−Au correlations in Pt$_{0.77}$Au$_{0.23}$, Pt$_{0.51}$Au$_{0.49}$, and Pt$_{0.40}$Au$_{0.60}$ NPs were eliminated and the Au−Au correlations extracted as follows

Au−Au partial PDF

$$= \frac{(\text{respective Total} G(r))}{w_{ij}} - \frac{(\text{respective DG}(r)_{Pt})}{\Delta w_{Pt-i}} \tag{9}$$

where w_{ij} and Δw_{Pt-i} are the weighting factors of the Pt−Pt and Pt−Au atomic pairs estimated using the respective definitions given in eqs 4 and 8 above. Note the derivation of the Au−Au partial PDF by eq 9 above is relatively straightforward in our case since both experimental PDF data sets involved in it have been derived from XRD data collected on the same instrument with similar statistical accuracy and to the same q_{max} value and have also been subjected to analogous correction and Fourier transformation protocols. The resulting Au−Au partial atomic PDFs for the 400 °C treated samples are shown in Figure 1a and those for the 800 °C treated samples are shown in Supporting Information Figure 6b. A comparison between the Au−Au partial PDFs for Pt$_{0.77}$Au$_{0.23}$, Pt$_{0.51}$Au$_{0.49}$, and Pt$_{0.40}$Au$_{0.60}$ NPs annealed at 400 and 800 °C is also shown in Supporting Information Figure S6.

Structure Modeling. The periodic (Bravais) lattice-constrained fitting of the experimental total PDFs was done with the help of the program PDFgui.[28] Data from literature sources[27] for the crystal structures of bulk Pt and Au were used as starting values in the fitting. It was done as to minimize a goodness-of-fit indicator, R_w, defined as

$$R_w = \left\{ \frac{\sum w_i (G_i^{exp} - G_i^{calc})^2}{\sum w_i (G_i^{exp})^2} \right\}^{1/2} \tag{10}$$

where G^{exp} and G^{calc} are the experimental and calculated PDFs, respectively, and w_i is the weighting factor reflecting the statistical quality of the individual data points. The structural parameters resulted from the fitting are summarized in Table 1.

Here it may be noted that the agreement factors achieved with the PDF fits based on lattice-type models are usually in the range of 15−20% as is the case with the present fits. Such R_w values appear somewhat high when compared to goodness-of-fit factors resulted from Rietveld refinement of XRD data in reciprocal space. This mostly reflects the fact that the atomic PDFs being fit take both the sharp, Bragg like features and the diffuse component of the XRD data into account while Rietveld fits consider only the former. The inherently higher absolute value of the goodness-of-fit factors in PDFs fits, however, does not affect their functional purpose as a residuals quantity that guides the refinement of the structural parameters of the tested Bravais lattices based models.

Finite size atomic configurations cut out of a perfect fcc-lattice (see Figure 2a) were used to start the reverse Monte Carlo simulations.[76] The configurations were spherical in shape and about 5.1 nm in diameter, that is, with a size and shape similar to those of the NPs studied here. In the simulations, the position of each atom from the approximately 5000 atom configurations was adjusted as to minimize the difference R_w (see eq 10 above) between the model and experimental PDF data. Atoms were constrained (i) not to come closer than preselected distances of closest approach and (ii) to maintain as maximal (i.e., as close to 12) as possible coordination numbers. The first constraint reflects the fact that, for example, Au atoms in the NPs studied do not approach each other closer than 2.6 Å as the experimental Au−Au partial PDFs show. The second constraint takes into account the close packing nature of the fcc-type atomic ordering in noble metals and their alloys. At the same time the energy of the configurations was optimized by minimizing pairwise (Lenard-Jones type) potentials for Pt and Au taken from literature sources.[77] The simulations were done with the help of a new version of the program RMC++[78] expanding on our recent work published in refs 26 and 79. The reverse Monte Carlo simulations refined structure models for Au and Pt NPs are shown in Figure 2c,d, respectively. These model configurations were used to produce the binary Pt−Au structure models in Figure 3 that show very different chemical ordered-disorder features.

ASSOCIATED CONTENT

Ⓢ Supporting Information
TEM, XRD, modeling and catalytic data. This material is available free of charge via the Internet at http://pubs.acs.org.

AUTHOR INFORMATION

Corresponding Author
*E-mail: petkov@phy.cmich.edu. Tel + 989 774 3395. Fax + 989 774 2697.

Author Contributions
V.P. performed the resonant high-energy XRD experiments and the structure modeling. C.J.Z., B.W., R.L., J.L. and L.Y. prepared the samples and did the TEM and catalytic activities characterization. S.S. developed the high-energy X-ray optics and organized/performed the XRD experiments.

Notes
The authors declare no competing financial interest.

ACKNOWLEDGMENTS

■ REFERENCES

(1) Lin, Ch.-An J.; Lee, Ch.-H.; Hsiech, J.-T.; Wang, H. H.; Li, J. K.; Shen, J. L.; Chan, W. H.; Yeh, H.-I.; Chang, W. H. *J. Med. Bio. Eng.* **2009**, *29*, 276−283.

(2) Daniel, M.Ch; Astruc, D. *Chem. Rev.* **2004**, *104*, 293−346.

(3) Mulvaney, P. *Langmuir* **1996**, *12*, 788−800.

(4) Alloyeau, D.; Ricolleau, C.; Mottet, C.; Oitkawa, T.; Langlois, C.; Bouar, Y.; Le, Braidy, N.; Loiseau, A. *Nat. Mat.* **2009**, *8*, 940−946.

(5) Boccuzzi, F.; Chiorino, A.; Manzoli, M.; Lu, P.; Akita, T.; Ichikawa, S.; Haruta, M. *J. Catal.* **2001**, *202*, 256−267.

(6) Luo, J.; Wang, L.; Mott, D.; Njoki, P. N.; Lin, Y.; He, T.; Xu, Zh.; Wanjana, B. N.; Lim, I.-Im; Zhong, Ch.-J. *Adv. Mater.* **2008**, *20*, 4342−4347.

(7) Esparza, R.; Ascencio, J. A.; Rosas, G.; Ramírez, J. F. S.; Pal, U.; Perez, R. *J. Nanosci. Nanotechnol.* **2005**, *5*, 641−647.

(8) Hvolbaek, B.; Janssens, T. V. W.; Clausen, B. S.; Falsig, H.; Christensen, C. H.; Norskov, J. K. *Nano Today* **2007**, *2*, 14−18.

(9) Marks, L. D. *Rep. Prog. Phys.* **1994**, *57*, 603−659.

(10) Petkov, V.; Bedford, N.; Knecht, M. R.; Weir, M. G.; Crooks, R. M.; Tang, W.; Henkelman, G.; Frenkel, A. *J. Phys. Chem. C* **2008**, *112*, 8907−8911.

(11) Huang, W. J.; Sun, R.; Tao, J.; Menard, L. D.; Nuzzo, R. G.; Zuo, J. M. *Nat. Mater.* **2008**, *7*, 308−313.

(12) Luo, J.; Maye, M. M.; Petkov, V.; Kariuki, N. N.; Wang, L.; Njoki, P.; Mott, D.; Lin, Y.; Zhong, Ch.-J. *Chem. Mater.* **2005**, *17*, 3086−3091.

(13) Xu, C.; Wang, R.; Chen, M.; Zhang, Y.; Ding, Y. *Phys. Chem. Chem. Phys.* **2010**, *12*, 239−246.

(14) Xiao, S.; Hu, W.; Luo, W.; Wu, Y.; Li, X.; Deng, H. *Eur. Phys. J.* **2006**, *B 54*, 479−484.

(15) Deng, L.; Hu, W.; Deng, H.; Xiao, S. *J. Phys. Chem. C* **2010**, *114*, 11026−11032.

(16) Leppert, L.; Kummel, S. *J. Phys. Chem. C* **2011**, *115*, 6694−6702.

(17) Braidy, N.; Purdy, G. R.; Botton, G. A. *Acta. Mater.* **2008**, *56*, 5972−5983.

(18) Vesnin, Y. I.; Shubin, Y. V. *J. Less-Common Met.* **1988**, *142*, 213−219.

(19) Petkov, V. *Mater. Today* **2008**, *11*, 28−38.

(20) Petkov, V.; Peng, Y.; Williams, G.; Huang, B.; Tomalia, D.; Ren, Y. *Phys. Rev. B* **2005**, *72*, 195402−7.

(21) Proffen, Th.; Petkov, V.; Billinge, S. J. L.; Vogt, T. *Z. Kristallogr.* **2002**, *217*, 47−50.

(22) Loffler, J.; Weismuller, J. *Phys. Rev. B* **1995**, *52*, 7076−7093.

(23) Egami, T. Billinge, S. J. L. In *Underneath the Bragg peaks*; Pergamon Press: New York, 2003.

(24) In *Fundamentals of x-ray crystallography*; Giacovazzo, G., ed.; Oxford University Press: New York, 1998.

(25) Gilber, B.; Huang, F.; Zhang, H.; Waychunas, G. A.; Banfield, J. F. *Science* **2004**, *305*, 651−654.

(26) Petkov, V.; Moreels, I.; Hens, Z.; Ren, Y. *Phys. Rev. B* **2010**, *81*, 241304−4.

(27) Wyckoff, R. W. G. In *Crystal Structures*, 2nd ed.; Interscience Publishers: New York, 1963.

(28) Farrow, C. L.; Juhás, P.; Liu, J. W.; Bryndin, D., E.; Božin, S.; Bloch, J.; Proffen, Th.; Billinge, S. J. L. *J. Phys.: Condens. Matter* **2007**, *19*, 335219−7.

(29) Sun, Y.; Zhuang, L.; Lu, J.; Hong, X.; Liu, P. *J. Am. Chem. Soc.* **2007**, *129*, 15465−15467.

(30) Menard, L. D.; Wang, Q.; Kang, J. H.; Sealey, A. J.; Girolami, G. S.; Teng, X.; Frenkel, A. I.; Nuzzo, R. G. *Phys. Rev. B* **2009**, *80*, 064111−11.

(31) Sanchez, S. I.; Small, M. W.; Zuo, J.-M.; Nuzzo, R. G. *J. Am. Chem. Soc.* **2009**, *131*, 8683−89.

(32) Small, M. W.; Sanchez, S. I.; Menard, L. D.; Kang, J. H.; Frenkel, A. I.; Nuzzo, G. R. *J. Am. Chem. Soc.* **2011**, *133*, 3582−3591.

(33) Fuoss, P. H.; Eisenberger, P.; Warburton, W. K.; Bienenstock, A. *Phys. Rev. Lett.* **1981**, *46*, 1537−1540.

(34) Laridjani, M.; Sadoc, J. F. *J. Non-Cryst. Solids* **1988**, *106*, 42−46.

(35) Matsubara, E.; Tamura, T.; Waseda, Y.; Zhang, T.; Inoue, A.; Masumoto, T. *J. Non-Cryst. Solids* **1990**, *150*, 380−385.

(36) Lima, de J.C.; Raoux, D.; Tonnerre, J. M.; Udron, D.; Machado, K. D.; Grandi, T. A.; de Campos, C. E. M.; Morrison, T. I. *Phys. Rev. B* **2003**, *67*, 094210−9.

(37) Petkov, V.; Shastri, S. D. *Phys. Rev. B* **2010**, *81*, 165428−8.

(38) Wurden, C.; Page, K.; Llobet, L.; White, C. E.; Proffen, Th. *J. Appl. Crystallogr.* **2010**, *43*, 635−638.

(39) Petkov, V.; Jeong, I.-K.; Chung, J. S.; Thorpe, M. F.; Kycia, S.; Billinge, S. J. L. *Phys. Rev. Lett.* **1999**, *83*, 4089−92.

(40) Sun, Ch.Q. *Nanoscale* **2010**, *2*, 1930−1961.

(41) Oezlasan, M.; Heggen, M; Strasser, P. *J. Am. Chem. Soc.* **2012**, *134*, 514−524.

(42) "There is Plenty of Room at the Bottom concept" of today's nanotechnology is credited to the physicist Richard Feynman at an American Physical Society meeting at Caltech on December 29, 1959.

(43) Kim, B. J.; Tersoff, J.; Wen, C.-Y.; Reuter, M. C.; Stach, E. A.; Ross, F. M. *Phys. Rev. Lett.* **2009**, *103*, 155701−4.

(44) Schwartz, R. B.; Khachaturyan, A. G. *Phys. Rev. Lett.* **1995**, *74*, 2523−26.

(45) Weissmuller, J; Lemier, Ch. *Philos. Mag. Lett.* **2000**, *80*, 411−418.

(46) Kuji, T.; Matsumura, Y.; Uchida, H.; Aizawa, T. *J. Alloys Compd.* **2002**, *330−332*, 718−722.

(47) Skulason, E.; Tripkovic, V.; Bjorketun, M. E.; Gudmundsdottir; Karlberg, G.; Rossmeisl, J.; Bligaard, Th.; Jonsson, H.; Norskov, J. K. *J. Phys. Chem. C* **2010**, *114*, 18182−18197.

(48) Crooks, R. M.; Zhao, M.; Sun, L.; Chevchik, V.; Yeung, L. K. *Acc. Chem. Res.* **2001**, *34*, 181−190.

(49) Witham, C. A.; Huang, W.; Tsung, Ch.-K.; Kuhn, J.; Somorjai, G. A.; Toste, F. D. *Nature Chem.* **2010**, *2*, 36−41.

(50) Casado-Rivera, E.; Volpe, D. J.; Aldem, L.; Lind, C.; Downie, C.; Vazquez-Alvarez, T.; Angelo, A. C. D.; DiSalvo, F. J.; Abruna, H. D. *J. Am. Chem. Soc.* **2004**, *126*, 4043−4049.

(51) Subhramannia, M.; Pillai, V. K. *J. Mat. Chem.* **2008**, *18*, 5858−5870.

(52) Miller, J.; Kropf, A.; Zha, Y.; Regalbuto, J.; Delannoy, L.; Louis, C.; Bus, E.; Vanbokhoven, J. *J. Catal.* **2006**, *240*, 222−234.

(53) Kang, J. H.; Menard, L. D.; Nuzzo, R. G.; Frenkel, A. I. *J. Am. Chem. Soc.* **2006**, *37*, 12068−69.

(54) Mukarjee, S.; Srinivasan, S.; Soriaga, M. *J. Electrochem. Soc.* **1995**, *142*, 1409−22.

(55) Chou, T. S.; Perlman, M. L.; Watson, R. E. *Phys. Rev. B.* **1976**, *14*, 3248−50.

(56) Rajasekharan, T.; Seshubai, V. *Acta Cryst. A* **2012**, *68*, 156−165.

(57) Tedsree, K.; Wong, Ch.; Chan, A.; Jones, S.; Cuan, Q.; Li, W.-K.; Gong, X.-Q.; Chi, S; Tsang. *Science* **2011**, *332*, 224−228.

(58) Berg, C.; Vevnik, H. J.; Stisland, F.; Ramstad, A.; Borg, A. *Surf. Sci.* **1998**, *409*, 1−15.

(59) Ge, Q.; Song, C.; Wang, L. *Comput. Mater. Sci.* **2006**, *35*, 247−253.

(60) Galvagno, S.; Parravano, G. *J. Catal.* **1979**, *57*, 272−286.

(61) Selvarani, G.; Selvaganesh, S. V.; Krishnamurthy, S.; Kiruthika, G. V. M.; Sridhar, P.; Pitchumani, S.; Shukla, A. K. *J. Phys. Chem. C* **2009**, *113*, 7461−7468.

(62) Dai, D.; Balasubramanian, K. *J. Chem. Phys.* **1994**, *100*, 4401−07.

(63) Tian, W. Q.; Ge, M.; Gu, F.; Yamada, T.; Aoki, Y. *J. Phys. Chem. A* **2006**, *110*, 6285−6293.

(64) Pedersen, M. O.; Helveg, S.; Ruban, A.; Stensgaard, I; Legsgaard, E.; Norskov, J. K.; Besenbacher, F. *Surf. Sci.* **1999**, *426*, 395−409.

(65) Mott, D.; Luo, J.; Njoki, P.; Lin, Y.; Wang, L.; Zhong, C. J. *Catal Today* **2007**, *122*, 378−385.

(66) Yuan, D.; Gong, X.; Wu, R. *J. Phys. Chem.* **2008**, *128*, 064706.

(67) Park, I.-S.; Lee, K-s.; Jung, D.-S.; Park, H.-Y.; Sung, Y.-E. *Electrochim. Acta* **2007**, *52*, 5599−5605.

(68) Xu, J. B.; Zhao, T. S.; Liang, Z. X. *J. Power Sources* **2008**, *185*, 857−861.

(69) Moussounda, P. S.; Haroun, M. F.; Legare, P. *Phys. Scr.* **2010**, *81*, 045603−5.

(70) Strasser, P.; Koh, S.; Anniyev, T.; Greeley, J.; More, K.; Yu, Ch.; Liu, Z.; Kaya, S.; Nordlund, D.; Ogasawara, H.; Toney, M. F.; Nillson, A. *Nature Chem.* **2010**, *2*, 454−460.

(71) Li, Y.; Samorjai, G. A. *Nano Lett.* **2010**, *10*, 2289−2295.

(72) Liu, Y.; Lowe, M. A.; DiSalvo, F. J.; Abruna, H. D. *J. Phys. Chem. C* **2010**, *114*, 14929−14938.

(73) Wanjala, B. N.; Luo, J.; Loukrakpam, R.; Mott, D.; Njoki, P. N.; Fang, B.; Engelhard, M.; Naslund, H. R.; Wu, J. K.; Wang, L.; Malis, O.; Zhong, C.-J. *Chem. Mater.* **2010**, *22*, 4282−4294.

(74) Falsig, H.; Hvolbek, B.; Kristensen, I. S.; Jiang, T.; Bligaars, Th.; Christensen, C. H.; Norskov, J. K. *Angew. Chem.* **2008**, *47*, 4835−4839.

(75) Shastri, S. D.; Almer, J.; Ribbing, C.; Cederström, B. *J. Synchrotron Radiat.* **2007**, *14*, 204−11.

(76) McGreevy, R. L.; Pusztai, L. *Mol. Simul.* **1998**, *1*, 359−67.

(77) Heinz, H.; Vaia, R. A.; Farmer, B. L.; Naik, R. R. *J. Phys. Chem. C* **2008**, *112*, 17281−17290.

(78) Gereben, O.; Jovari, P.; Temleitner, L.; Pusztai, L. *J. Optoelectron. Adv. Mater.* **2007**, *9*, 3021−7.

(79) Welborn, M.; Tang, W.; Ryu, J.; Crooks, R. M.; Petkov, V.; Henkelman, G. *J. Chem. Phys.* **2011**, *135*, 014503−5.